

A Coupled Model for the Simulation of Miniaturized and Integrated Photoacoustic Gas Detector

A. Glière · J. Rouxel · B. Parvitte · S. Boutami · V. Zéninari

Received: 6 May 2013 / Accepted: 1 November 2013 / Published online: 23 November 2013
© Springer Science+Business Media New York 2013

Abstract In photoacoustic (PA) spectroscopy, the signal is inversely proportional to the resonant cell volume. This favorable scaling behavior has provoked in recent years a growing interest in the miniaturization of PA cells. Due to dimension downscaling, technological constraints, and preliminary design choices, the modeling hypotheses used at the macro-scale are no longer valid. Here, a new model adapted to miniaturized and integrated PA (μ -PA) sensors is presented. The coupled model takes advantage of commercial software to address, respectively, (i) the electromagnetic mode propagation in the waveguide, (ii) the mid-IR light illumination of the chamber and its interaction with the molecules of interest, and (iii) the creation and propagation of acoustic waves in the cell. The model has been used to confirm the validity of the choice of the differential Helmholtz resonator principle and to provide a prototype μ -PA cell geometry. It is shown that, in spite of the specific issues inherent to miniaturization and integration, in particular, the strong divergence of the light beam and the crucial influence of viscothermal dissipation processes, the μ -PA sensor produces a pressure signal compatible with the next generation of resonant microphone technology. The model will be further improved when measurements performed on the prototype currently in fabrication are available.

Keywords Finite element method · Photoacoustic spectroscopy · Raytracing · Simulation · Viscothermal acoustics

A. Glière (✉) · J. Rouxel · S. Boutami
CEA, LETI, MINATEC Campus, 17 rue des Martyrs,
38054 Grenoble Cedex 9, France
e-mail: alain.gliere@cea.fr

J. Rouxel · B. Parvitte · V. Zéninari
Groupe de Spectrométrie Moléculaire et Atmosphérique,
UMR CNRS 7331, Faculté des Sciences, Université de Reims, Moulin de la Housse,
51687 Reims Cedex 2, France

1 Introduction

Among optical gas sensing methods, photoacoustic (PA) spectroscopy combined with a laser source has proven to be a very robust and sensitive method for trace gas detection [1,2]. In PA spectroscopy, the light source is modulated at an acoustic frequency. This modulation creates a periodic variation of temperature in the absorption cell due to non-radiative relaxation of excited molecules, and thus an acoustic wave [3,4]. This method has the advantages of high sensitivity, high dynamic range, and ease of use. Moreover, the device sensitivity can be improved by the use of a resonant absorption cell. PA sensors work at atmospheric pressure as well as at reduced pressure [4]. The laser wavelength is chosen to correspond to a strong absorption line of the molecule to detect. Mid-infrared (mid-IR) lasers have commonly been used for gas measurement in the rotational–vibrational transition range, which is the spectral range of fundamental absorption bands of most atmospheric constituents [3]. Quantum cascade lasers (QCL) [5] are very suitable for such applications because they are at present the only semiconductor laser sources operating in the mid-IR wavelength range at room temperature. Compact, robust, and low-cost distributed feedback QCL are available for continuous wave operation [2,6].

For trace gas measurements, the PA signal is directly proportional to the absorption coefficient of the molecules, to the radiation power, and to the cell response. The latter is inversely proportional to the cell volume [4]. This favorable scaling behavior has provoked in recent years a growing interest in the miniaturization of PA cells for gas sensing.

A first technique developed to reduce the size of the PA sensors is called quartz-enhanced photoacoustic spectroscopy (QEPAS) [7]. It consists in replacing the acoustic transducer by a tiny quartz tuning fork, such as that commonly used in electronic wristwatches, with a resonant frequency around 33 kHz in vacuum and an extremely high quality factor ($\sim 10^4$ at atmospheric pressure). In QEPAS, the PA energy is accumulated in the sharply resonant tuning fork, instead of in the cell as in traditional PA spectroscopy, as oscillations which generate a current signal by the piezoelectric effect. The piezoelectric current signal is then transformed to a voltage signal by a transimpedance amplifier and further demodulated by a lock-in amplifier.

An alternative technique consists in the miniaturization of a standard macro-scale PA cell. One can particularly cite the work of Firebaugh [8], later carried on by Pellegrino and Holthoff [9]. Addressing the detection of chemical agents, they designed and characterized a differential cell of $\sim 15 \text{ mm}^3$ internal volume and a detection limit of ~ 20 ppb for dimethyl methylphosphonate (DMMP). Other notable progress in the size reduction direction has also been performed by Gorelik et al. [10] with inclined geometry cells, as small as $\sim 500 \text{ mm}^3$ internal volume, with a detection limit of ~ 10 ppm for ammonia or by Karioja et al. [11] with a differential PA cell made with low-temperature co-fired ceramics technology.

Our original approach aims at demonstrating the feasibility of a miniaturized and fully integrated optical gas sensor including a mid-IR QCL and a Helmholtz resonant PA sensor combined with microelectromechanical systems (MEMS) microphones and their readout electronics [12]. The main objective of the integration on the silicon planar substrate is to address the low-cost market and mass deployment, for example, for use

in greenhouse gas measurement networks, indoor air quality assessment, or industrial process monitoring. Compatibility with integrated circuits and MEMS microfabrication technologies must be ensured from the very beginning of the device design.

This paper presents a new coupled optics–acoustic model for the simulation of future miniaturized and integrated PA gas detectors. It places a particular emphasis on the coupling efficiency between mid-IR radiation, gas, and acoustics. The microphone influence on the acoustic behavior of the cell is not considered at this stage.

2 Miniaturized and Integrated Differential Helmholtz Resonator

A Helmholtz resonator consists of a closed volume associated with a capillary. It is the acoustic equivalent of a simple mechanical oscillator composed of a mass and a spring. The air in the closed volume plays the role of the spring, while the air in the capillary corresponds to the moving mass. It is possible to enhance significantly the Helmholtz resonator sensitivity and signal-to-noise ratio by using the differential scheme, consisting of two identical chambers connected by two capillaries [13]. At the resonant frequency, the gas in the capillaries moves like a piston compressing the gas in one chamber of the PA cell while expanding it in the other. Although only one chamber of the PA detector is illuminated by a laser beam, acoustic waves, opposite in phase at the Helmholtz resonance frequency, are generated in both chambers of the detector. The signals from microphones measuring the pressure in each chamber may be subtracted by a differential amplifier, thus doubling the valid signal and, correspondingly, the sensitivity of the PA Helmholtz resonator. Furthermore, the resulting differential Helmholtz resonator (DHR) (i) allows significant suppression of the in-phase external acoustic noise, which is an important part of the noise of PA detectors at atmospheric pressure and (ii) is relatively insensitive to the shape of the laser illumination because the overlap integral of the fundamental mode is quite constant in the illuminated chamber [14, 15]. Of course a few drawbacks, such as the low value of the quality factor, smaller than 10, are expected.

PA spectroscopy behaves favorably when the cell size is decreased and the individual components of the PA sensor, such as QCL sources [6], mid-IR waveguides [16], and MEMS microphones [17], are becoming available in CMOS compatible technologies. Therefore, time comes for engaging a DHR-based sensor in the process of dramatically miniaturizing and fully integrating in silicon technologies. From now on, this sensor is referred to as the μ -PA sensor. As compatibility between MEMS and CMOS integrated circuits processes is ensured, the sensor readout electronic circuit can also be integrated on the chip.

Of course, using the CMOS compatible MEMS technologies places numerous constraints on the device design, which must be devised together with the microfabrication flow. This co-design process is not discussed here but some of its consequences, relevant for the model, are listed. First, the deep reactive ion etching process, typically used to dig high aspect ratio structures, such as the PA cell, produces flat faces. Therefore, the cylindrically shaped cavities and capillaries usually employed in a macro-sized PA cell must be replaced by parallelepipeds. Second, the chamber should fit in a wafer thickness. Third, from the technological point of view, the fabrication of structures

having comparable size but different depth, as required to form the cavities and the capillaries, is extremely difficult, if not impossible. To ensure dimensional control and process reproducibility, the fabrication of the cavities and the capillaries should be split on two separate wafers, one of them being used to seal the entire structure. Fourth, for technological reasons, the mid-IR waveguide is typically buried under a relatively thin layer of silicon ($\sim 10 \mu\text{m}$) so that the laser beam enters the cavity close to its bottom. Finally, in order to improve the process robustness, the MEMS microphones are built in a separate wafer. This third wafer constitutes the cell floor. A schematic view of the μ -PA cell is presented on Fig. 1.

It is not economically viable to build and test a large number of different DHR cells and then compare their detection capabilities since the technologies required for their fabrication are expensive and time consuming. Resorting to modeling and numerical simulation is a way to get over some of these limitations. A new coupled model adapted to miniaturized and integrated PA sensors has thus been developed. It addresses (i) the electromagnetic mode propagation in the waveguide, (ii) the light illumination of the chamber, (iii) the interaction of mid-IR light with the molecules of interest, and

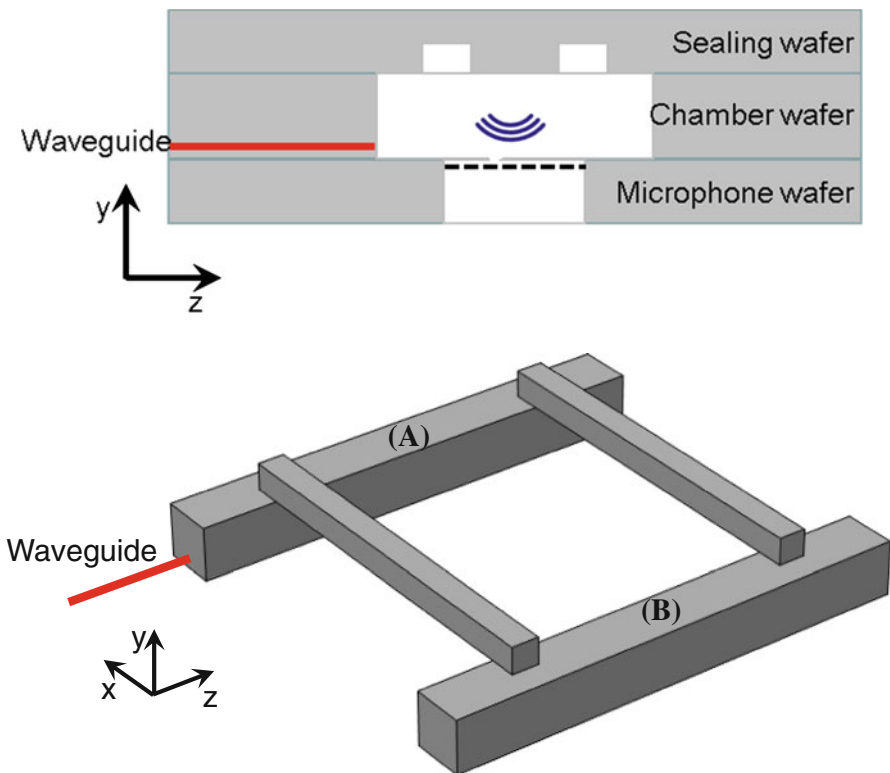


Fig. 1 Schematic view of the μ -PA DHR cell constituted by a stack of three wafers (*top*) and CAD model with reference axes (*bottom*). The illuminated chamber is referred to as chamber A while the non-illuminated chamber is referred to as chamber B

(iv) the creation and propagation of acoustic waves in the cell. The microphone influence and response are not considered at this stage.

3 Optical Model

A basic optical model is generally used at the macro-scale to calculate the photon energy flux. Namely, the laser illumination geometry is assimilated to a straight beam for which the flux has a Gaussian distribution within a cross section [18–20].

However, several specific problems arise when miniaturizing PA cells and integrating them in a planar substrate by MEMS technologies. First, the mid-IR radiation is injected in the chamber by means of a waveguide, whose height and width are of the order of the radiation wavelength. The beam is diffracted and is thus strongly divergent. Second, silicon is transparent to mid-IR radiation and the natural confinement of energy, which is obtained by reflexion on the metallic walls of macro-size devices, is not present. Finally, in the DHR configuration, a portion of the light emitted by the laser source can be refracted toward the non-illuminated chamber and interacts there with the gas. This crosstalk between chambers can adversely affect the detector performance.

Due to the abovementioned problems, the basic optical model obviously collapses when the device is miniaturized and integrated in silicon. A more sophisticated model, made up of two parts, respectively, accounting for the propagation of the electromagnetic field in the waveguide and in the chamber, must be devised.

3.1 Waveguide Model

The SiGe/Si waveguide [16] is designed to be monomodal at the wavelength of interest. The fundamental mode propagating in the waveguide is calculated in TM polarization using the beam propagation method (BPM) [21], implemented in the BeamPROP commercial software (Rsoft Design Group, Ossining, NY, USA). The choice for this polarization is due to the fact that the waveguide is meant to be coupled to a QCL, the latter operating in TM polarization. The map of the y component of the mode electric field is presented on Fig. 2 (left).

3.2 Propagation and Absorption of the Mid-IR Light in the Chamber

Due to the very large length scale ratio between the size of the device (the chamber is several millimeters long) and the mid-IR wavelength (e.g., 4.2 μm for CO_2 detection), the computation of the propagation of the electromagnetic field in the chamber by an exact solution of Maxwell's equations cannot be solved on easily available workstations and is thus not practical. The exact solution methods, whether they are based on volume discretization, such as the finite difference time domain method or the finite element method, or surface discretization, such as the boundary element method, would lead to huge algebraic systems because the mesh size must be much smaller than the radiation wavelength.

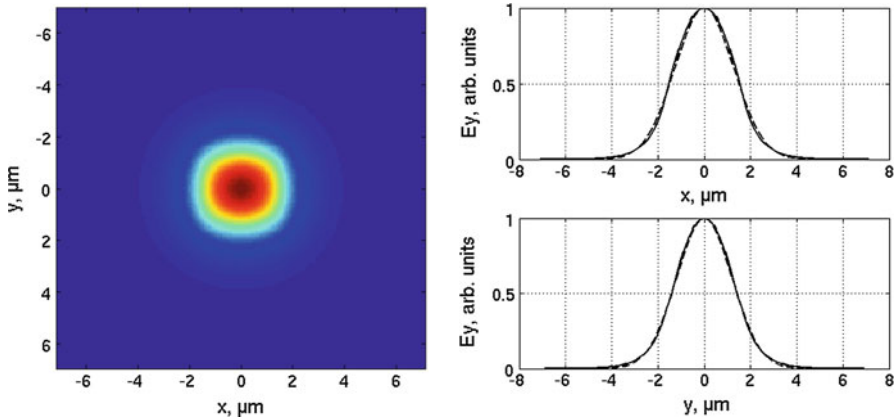


Fig. 2 TM-polarized fundamental mode propagating in the waveguide (4.2 μm wavelength). Map of the y component of the electric field (left) and Gaussian fit (right). Mode profile (solid line) and Gaussian fit along x and y axes (dashed line)

However, in this case, the propagation of light can be simply modeled by geometric optic tools (raytracing method), which are less computationally demanding than full-wave electromagnetic simulations, while providing almost as accurate results. Using the raytracing method implies that no sub-wavelength features, able to diffract light, are present in the system. Only reflection and refraction at locally plane interfaces are taken into account. The method of choice is the combination of raytracing with the Monte Carlo method [22, 23]: a large number of rays are followed individually from their random generation at the light source to their exit of the domain.

To make the connection between light inside the waveguide and the light source in the chamber, one needs to convert the single mode exiting the waveguide to plane waves (i.e., rays) by a two-dimensional Fourier transform of the electric field repartition at the waveguide exit section [24]. For this purpose, the guided mode is fitted to a Gaussian mode, the agreement being very good due to the mode confinement chosen (Fig. 2, right). The Fourier transform of the spatial mode distribution can then be performed analytically and provides a two-dimensional Gaussian representing the angular and amplitude dispersion of rays illuminating the chamber:

$$\hat{I}(p, q) = I_0 \frac{w_{0x} w_{0y}}{4\pi} e^{-\left(\frac{k^2 w_{0x}^2}{8} p^2 + \frac{k^2 w_{0y}^2}{8} q^2\right)}, \tag{1}$$

where p and q are the direction cosines of the ray, k is its wavenumber, and w_{0x} and w_{0y} are the Gaussian beam waists along x and y axes. Gaussian widths in the Fourier domain are inversely proportional to Gaussian widths in the spatial domain, as shown in the above equation. From a practical point of view, a large number of rays are randomly sent from the exit section of the waveguide, with directions and amplitudes corresponding to the Gaussian distribution in Fourier space. It is worth noting that, if the mode is not well confined, the profile might notably differ from a Gaussian and the Fourier transform has thus to be performed numerically.

The polarization state of each ray is derived from its wavevector \mathbf{k} and the fact that the electric field is oriented along the \mathbf{y} vector at the waveguide exit (TM polarization). The electric field is oriented along the \mathbf{p} vector defined by

$$\begin{aligned} \mathbf{s} &= \mathbf{y} \times \mathbf{k} \\ \mathbf{p} &= \mathbf{k} \times \mathbf{s} \end{aligned} \quad (2)$$

When a ray hits an air-silicon interface, it is randomly reflected or refracted, following the polarization-dependent Fresnel equations.

Due to interaction with gas molecules, the ray energy is partially absorbed along its path. The physics of interaction between the IR radiation and the gaseous compound of interest has been presented by several authors in the PA detection context [25] and can be summarized as follows:

- The absorption of a photon by a molecule leads to the excitation of rotational or vibrational energy levels. The energy of mid-IR photons is not sufficient to excite electronic energy levels.
- Rotational and vibrational states lose their energy by collisional relaxation, and heat (translational energy) is released.
- In the mid-IR range, other relaxation processes, such as radiative emission, photochemistry, etc., are either impossible or unlikely and can thus be neglected.

The complex cascade of physical phenomena is thus considerably simplified, and it is assumed that the whole energy of the absorbed photons is released locally as heat [4]. Moreover, in the context of mid-IR PA gas detection, it is reasonable to suppose that the absorption transition is not saturated by a strong photon flux and that the light source modulation is slow in comparison with the collisional relaxation processes [18]. Finally, the local heat source is directly proportional to the photon energy flux I , the absorption cross section σ , and the concentration n of the molecules of interest:

$$\frac{dI}{dx} = -I n \sigma \quad (3)$$

The local energy deposition along the ray path is computed by the Beer–Lambert law, which is the integral version of the above equation, and recorded for later use as a heat source in the acoustic model.

The raytracing model is implemented using the non-sequential mode of the commercial software Zemax (Radiant Zemax, Redmond, WA, USA). Two chambers are immersed in a bounding silicon volume whose external boundary is absorbing (Fig. 3). A rectangular source is positioned at the edge of the illuminated chamber, 10 μm above the chamber bottom. The wavelength of the TM-polarized source is 4.2 μm . The Gaussian mode has 1.79 μm and 1.69 μm waists, respectively, along the x and y axes. The optical index of silicon is excerpted from the software materials database. The absorption coefficient due to CO_2 in air at atmospheric pressure is set to 0.1 cm^{-1} . The energy deposition is recorded in $5 \times 5 \times 5 \mu\text{m}^3$ voxels. A convergence study shows that emitting 10^8 rays results in a good accuracy versus CPU time trade-off.

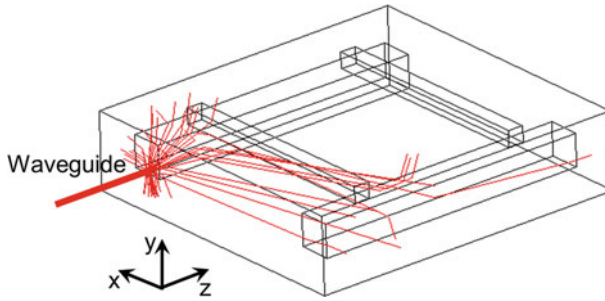


Fig. 3 Raytracing in the μ -PA DHR cell. Crosstalk appears when light emitted by the laser source is refracted toward the non-illuminated chamber, where it can interact with the gas

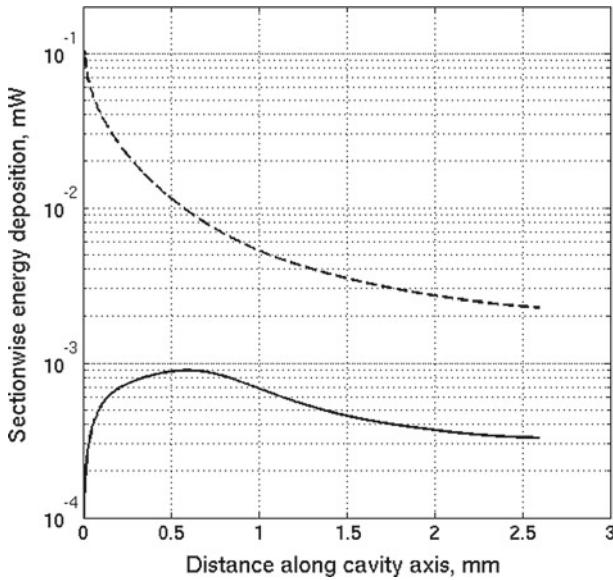


Fig. 4 Sectionwise energy deposition profile along the illuminated (*dashed line*) and the non-illuminated chamber (*solid line*). The plotted data represent the absorbed energy integrated on s sections (i.e., voxel layers) in the $x - y$ plane. The emitted power is 1 mW, and the computation is performed with 10^8 rays

As can be seen in Fig. 4, where energy profiles, integrated on cross sections perpendicular to the z axis, are presented, the energy absorbed in the illuminated chamber is mostly located close to the waveguide exit and a small, but still significant, part of the energy is deposited in the non-illuminated chamber.

4 Viscothermal Acoustic Model

The pressure acoustic model is commonly used to simulate the PA device behavior [18,20,26]. It is derived from the first principles governing equations, namely, the mass, momentum, and energy conservation laws supplemented with a thermodynamic

equation of state. Assuming adiabatic propagation in an ideal lossless gas and after some manipulation, a single inhomogeneous Helmholtz equation for the unknown pressure is obtained [27].

However, various volume and surface dissipation processes are at work in the gas, respectively, in the bulk of the propagation medium and close to the cell walls [4, 27]. The latter are of utmost importance in miniaturized PA devices. They occur by viscous dissipation and heat conduction in thin boundary layers located near the cell walls. In the interior of the cell, the gas acoustic velocity is proportional to the pressure gradient whereas at the wall, the no-slip boundary condition imposes a null tangential component. Thus, viscous dissipation occurs in a transition region, the viscous boundary layer. Similarly, the thermal boundary layer is the transition region where the adiabatic expansion and contraction of gas occurring in the interior of the cell, turns to isothermal, due to the high thermal conductivity of the cell walls relative to that of the gas. The values of the thicknesses d_μ and d_κ of the viscous and thermal boundary layers are roughly equal in air. They are given by

$$d_\mu = \sqrt{2\mu/\rho\omega} \quad (4)$$

$$d_\kappa = \sqrt{2\kappa/\rho C_p\omega}, \quad (5)$$

where μ , ρ , κ , and C_p are, respectively, the shear dynamic viscosity, mass density, thermal diffusivity, and heat capacity at constant pressure of the gas and ω is the angular frequency of the sound wave. As shown by Eqs. 4 and 5, the thickness of the boundary layers is inversely proportional to the square root of the sound wave frequency. In air, the values of d_μ and d_κ are similar.

The pressure acoustic model can be adapted as follows to approximately take into account the volume and surface dissipation effects [18, 28]: the pressure field is expressed as a series expansion in the eigenmodes of the PA cell, and quality factors, corresponding to the various volume and surface loss mechanisms, are introduced in the amplitude of the eigenmodes. It has recently been shown that this improved pressure acoustic model can accurately predict quality factors and resonance frequencies of a DHR at the macro-scale [20]. Obviously however, this method cannot help assess the resonance frequency shift due to losses. Since the boundary layers are thin in comparison with macro-size cell dimensions, an alternative approach, consisting of incorporating the effect of dissipation processes in especially designed boundary conditions, has been devised [19].

In a miniaturized DHR device such as the one studied here, with a working frequency around 20 kHz and in air at atmospheric pressure, the boundary layer thicknesses are in the 15 μm to 20 μm range, which is of the same order of magnitude as the capillary side length. Consequently, the viscous and thermal dissipation phenomena occurring close to the walls become essential and the pressure acoustic model must be abandoned in favor of a more sophisticated one. It is worth noting that, in their study of two MEMS scale PA devices, Holthoff et al. [26] compared simulation results, obtained with the pressure acoustic model, to measurements of the resonance frequency and emphasized that the discrepancies found were unacceptable. The dimension of their resonators was nevertheless quite larger than the one currently under consideration.

In the last decade, a lot of effort has been devoted in computational acoustics to the creation of computationally efficient models that are either approximate [29,30] or limited to certain classes of geometries [31].

In this work, in order to avoid restrictive assumptions when addressing miniaturized devices, but in exchange for more important computational cost, the full set of mass, momentum, and energy conservation equations is dealt with [32,33]. Of course, it should be kept in mind that the continuum physics framework used in our reasoning would collapse if the mean free path of gas molecules and molecular relaxation time are no longer small compared to other length and time scales of the system. This would occur in rarefied gas or if dimension downscaling were carried further.

Small harmonic variations of the variable density ρ , velocity \mathbf{u} , pressure p , and temperature T fields, are assumed:

$$\rho = \rho_0 + \tilde{\rho} \quad (6)$$

$$\mathbf{u} = \mathbf{u}_0 + \tilde{\mathbf{u}} \quad (7)$$

$$p = p_0 + \tilde{p} \quad (8)$$

$$T = T_0 + \tilde{T}, \quad (9)$$

where ρ_0 , p_0 , \mathbf{u}_0 , and T_0 are the mean values of the fields and the tilde capped variables are the corresponding unknown acoustic variables. From this point, it is assumed that the fluid is at rest, that is, $\mathbf{u}_0 = 0$.

Using the ideal gas equation of state,

$$p = \rho R_M T, \quad (10)$$

where R_M is the specific gas constant, the following set of harmonic linearized partial differential equations (PDEs) can be derived:

$$i\omega \left(\frac{\tilde{p}}{\rho_0} - \frac{\tilde{T}}{T_0} \right) + \nabla \cdot \tilde{\mathbf{u}} = 0 \quad (11)$$

$$i\omega\rho_0\tilde{\mathbf{u}} = -\nabla\tilde{p} + \nabla \cdot (\mu(\nabla\tilde{\mathbf{u}} + \nabla\tilde{\mathbf{u}}^T) + (\lambda - 2\mu/3)(\nabla \cdot \tilde{\mathbf{u}})\mathbf{I}) \quad (12)$$

$$i\omega\rho_0 C_p \tilde{T} = -\nabla \cdot (-\kappa\nabla\tilde{T}) + i\omega\tilde{p} + Q, \quad (13)$$

where λ and μ are the bulk viscosity and shear dynamic viscosity and Q is the heat source. In fact, it is possible to further simplify the problem and eliminate the pressure variable but this may lead to numerically unstable numerical schemes [33].

To close the definition of the problem, a set of boundary conditions must be applied. Due to the choice of the formulation, general boundary conditions could be used but it is assumed in this work that the cell walls are sound hard, subjected to a no-slip condition and isothermal.

The set of PDEs (Eqs. 11–13) and associated boundary conditions are solved by the finite element method (FEM), using the commercial software Comsol Multiphysics (Comsol AB, Stockholm, Sweden). One of the benefits of the FEM is its ability to handle any cell geometry. The studied domain is the DHR interior composed of two chambers linked by two capillaries (Fig. 1). It is assumed that the microphone does

not affect the acoustic behavior of the cell. The physical properties of air at standard ambient temperature and pressure are taken from the software material database. The bulk viscosity is set to 0.6μ [31]. Depending on the wanted results, either a harmonic solution combined with a frequency sweep or an eigenfrequency solution is performed.

Designing the FEM mesh is the object of special care as the rapid variation of the unknown variables in the thermal and viscous boundary layers must be accounted for [32]. Several layers of triangular prismatic elements are placed on the cell walls, and the cell interior is meshed with a tetrahedron. A mesh convergence study has shown that (i) it is sufficient to place two layers of elements in the boundary layer and that (ii) it is necessary to finely mesh the whole cell walls, not only the capillary walls.

The coupling with the optical model described in the previous section occurs through the heat source term of the energy conservation equation (Eq. 13). For this purpose, (i) the total emitted power is scaled linearly and (ii) the deposited energy density, recorded on voxels located on a regular three-dimensional grid, is interpolated on the unstructured FEM mesh.

5 Results

The model described in the previous sections has first been used to design a prototype of the μ -PA cell. Then, motivated by the specific features of the μ -PA cell, the analyses of the effect of the localization of the energy deposition and of the crosstalk between chambers have been carried out.

5.1 Design of a Prototype μ -PA Cell

A macro-size DHR cell has been designed, characterized, and used in the last decade for trace gas monitoring at GSMA laboratory [13,34]. The approach used to design a miniaturized version of this device, in compliance with the technological constraints listed in Sect. 2, is presented here. In a first step, the homothetic scaling down of the macro-size DHR by a factor of roughly 40 has been assessed. In a second step, the design has been improved. An arbitrary limit has been set at 20 kHz on the resonance frequency because the light source modulation must be kept much slower than the collisional relaxation process in order to preserve signal linearity. The characteristic dimensions of the macro-size DHR, the homothetic cell, and the improved μ -PA cell are summarized in Table 1. The chambers and capillaries of the macro-size DHR are cylinders defined by their length and diameter. The chambers and capillaries of the

Table 1 Dimensions of the macro-size DHR, the homothetic cell, and the improved μ -PA cell

Dimension (mm)	Macro-size DHR	Homothetic cell	μ -PA cell
Chamber length	102	2.6	2.6
Chamber cross section	10.8	0.3	0.3
Capillary length	84	2.1	2.1
Capillary cross section	2.06	0.05	0.15

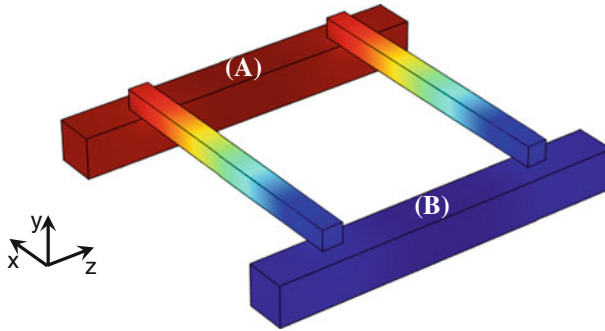


Fig. 5 Fundamental resonance mode in the μ -PA cell. High pressure in the illuminated chamber A (*red*) and low pressure in the non-illuminated chamber B (*blue*). Ideally, the pressure in chambers A and B should be in opposite phases (Color figure online)

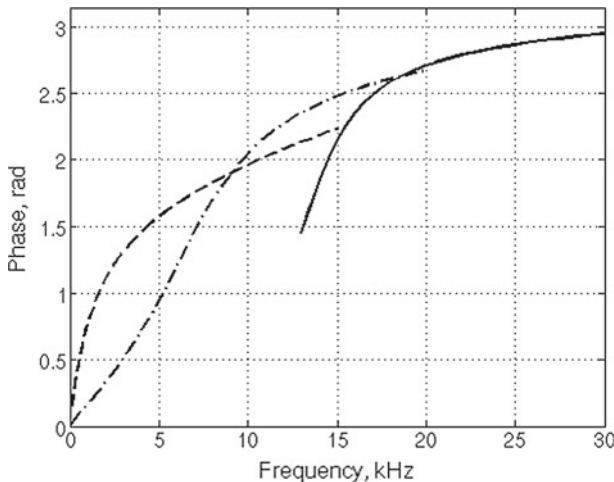


Fig. 6 Phase difference between pressure signals in chambers A and B for 50 μm (*dashed line*), 80 μm (*dashed-dotted line*), and 150 μm (*solid line*) capillary side length

miniaturized cells are square cross section parallelepipeds, defined by their length and the square side length.

A 1 mW laser source is uniformly spread in chamber A, and the gas absorption coefficient is set to 0.1 cm^{-1} . It is assumed that the pressure is measured at the center of the bottom face of the chambers. This hypothesis does not affect the value of the pressure signal as the pressure field is almost constant in each chamber (Fig. 5). The signal of interest is the amplitude of the difference between the pressures measured in both chambers.

Ideally, for the DHR principle to function properly, the pressure in the illuminated chamber A and the non-illuminated chamber B should be in opposite phases but the phase opposition in the homothetically scaled version of the DHR cell is not satisfactory (Fig. 6, dashed line). The phase opposition has been improved by increasing the capillary side length from 50 μm to 80 μm and finally to 150 μm (solid line). The

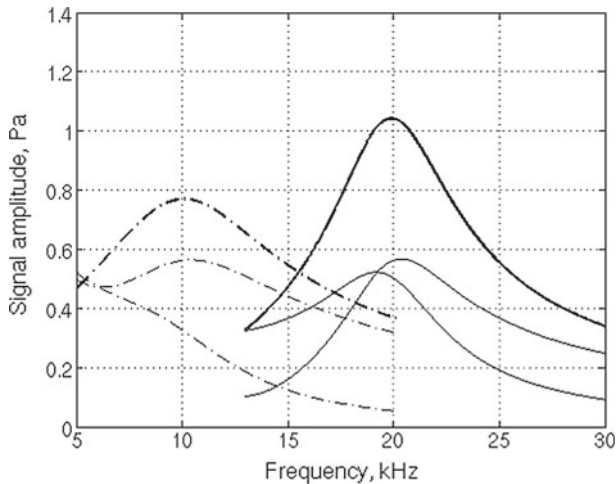


Fig. 7 Amplitude of the pressure signals for 80 μm (dashed–dotted line) and 150 μm (solid line) capillary side length. Signals in chambers A and B (thin lines) and difference signal (thick lines)

side length was not increased further because the peak signal frequency increases in parallel.

The improved μ -PA design, with a 150 μm side length delivers a 1.04 Pa difference pressure signal at 19.9 kHz, with a quality factor value of 1.99 (Fig. 7, solid line). Its dimensions are summarized in the third column of Table 1.

5.2 Localization of the Energy Absorption

As can be seen in Fig. 4, most of the interaction of mid-IR radiation with the gas of interest happens close to the waveguide exit. This motivates a study of the influence of the localization of the energy absorption on the behavior of the μ -PA cell. In addition to the energy repartition obtained by raytracing, two ideal cases are studied: a uniform and a Gaussian repartition. In the uniform repartition case, the absorbed energy is constant in space. In the Gaussian repartition case, the absorbed energy follows a two-dimensional Gaussian profile in the $x - y$ plane and is constant along the z axis. As noted previously, 1 mW laser source is injected and the absorption coefficient is set to 0.1 cm^{-1} .

The results are presented in Fig. 8. Due to its divergence at the waveguide exit, the beam energy is clearly not used at its best: 4.6 μW only are absorbed, and the corresponding signal is 0.176 Pa (\blacktriangle). If a uniform illumination (\blacksquare) or a Gaussian beam (\bullet) is considered, the absorbed energy is 26 μW and the signal is, respectively, 1.04 Pa and 1.18 Pa. The superior yield of the Gaussian beam is probably due to the fact that the interaction occurs away from the walls, where the major part of the dissipation is located. The sensor would clearly benefit from an improved coupling of light with gas in the chamber: it is necessary to inject 5.6 mW from the waveguide (\triangle), corresponding to the same energy deposited in the chamber, to obtain a signal similar to the ones obtained for uniform or Gaussian illuminations.

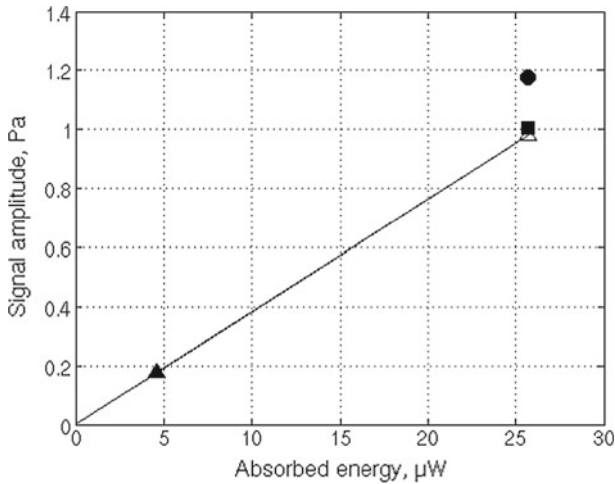


Fig. 8 Study of the absorbed energy localization on the pressure difference signal. Uniform illumination (■), Gaussian beam (●) and waveguide (▲) for a 1 mW source. Waveguide source computed with the same absorbed energy as the uniform and Gaussian sources (△)

5.3 Crosstalk Between Chambers

As can be seen in Figs. 3 and 4, due to the transparency of silicon to mid-IR radiation, a small part of the light emitted by the laser source is refracted toward the non-illuminated chamber, where it can interact with the gas. This is what we refer to as crosstalk. In fact, when 1 mW enters the illuminated chamber, 4.7 μW are deposited there and 0.29 μW are deposited in the other chamber. The ratio of energy deposited in chambers A and B is thus $\sim 6\%$.

The comparison between the cases with (solid line) and without (dashed lines) crosstalk is presented in Fig. 9. The influence of crosstalk is moderate: peak signal frequency and quality factor remain unchanged while the peak signal amplitude is decreased by $\sim 7\%$.

In order to assess the influence of the localization of energy deposition on crosstalk, the case where energy deposition is uniform in both chambers has also been studied (Fig. 10). As noted previously, the ratio of energy deposited in the illuminated and the non-illuminated chambers is $\sim 6\%$. The same conclusion can be drawn regarding the resonance frequency, quality factor, and maximum signal amplitude.

At this point, the microphone resolution necessary to meet the sensor specification can be assessed. Typically, the sensor should detect 1 ppm variation of concentration in air at standard ambient temperature and pressure, where around 400 ppm of CO_2 are present. Assuming a value of 0.1 cm^{-1} for the absorption coefficient, the value of the peak signal, with crosstalk taken into account, is 0.163 Pa. The microphone resolution should then be lower than 23 dB (ref. 20 μPa RMS). This is a challenging objective as, with ~ 30 dB resolution, MEMS microphones commonly used in mobile phones do not meet this requirement. However, a new generation of resonant microphones, using piezo-resistive silicon nanogauges [35] has the capability to match this resolution.

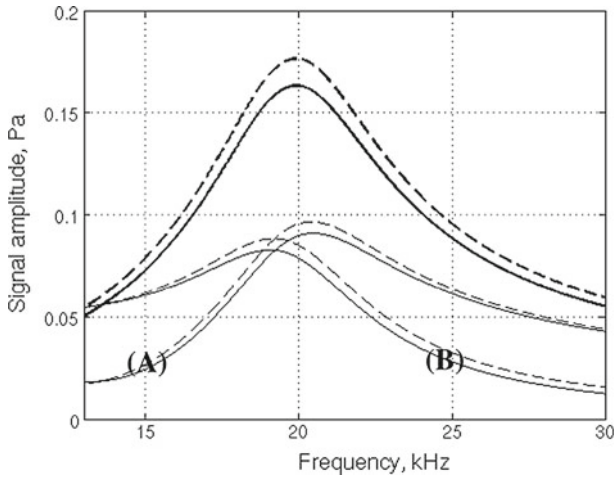


Fig. 9 Influence of crosstalk on the amplitude of the pressure signal. Computations with (*solid line*) and without (*dashed lines*) crosstalk. The *thick lines* correspond to the difference signal whereas the *thin lines* correspond to the signal in the A and B chambers

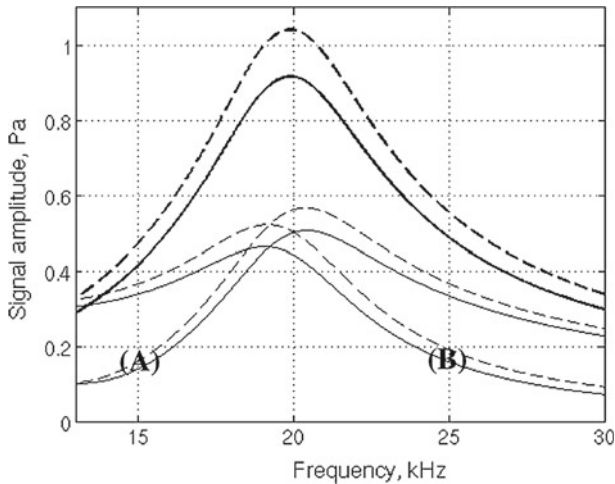


Fig. 10 Influence of crosstalk with uniform energy deposition on the amplitude of the pressure signal. Computations with (*solid line*) and without (*dashed lines*) crosstalk. The *thick lines* correspond to the difference signal whereas the *thin lines* correspond to the signal in A and B chambers

It is also worth noting that a 1 mW power waveguide output is a very conservative assumption.

6 Conclusion

When compared to macro-size ones, miniaturized and integrated PA (μ -PA) sensors have distinctive features that have a strong impact on the models used for their design.

On the optical model side (i) the mid-IR radiation, injected in the chamber by means of a waveguide is strongly divergent, (ii) silicon is transparent to mid-IR radiation, and (iii) crosstalk between chambers can adversely affect the detector performances. On the acoustic model side, the viscous and thermal dissipation phenomena occurring close to the μ -PA cell walls become essential. Therefore, models valid at the macro-scale are not adapted to μ -PA sensors and a dedicated coupled model has been developed. This model addresses (i) the electromagnetic mode propagation in the waveguide, (ii) the light illumination of the chamber, (iii) the interaction of mid-IR light with the molecules of interest, and (iv) the creation and propagation of acoustic waves in the cell.

Using the coupled model, the validity of the choice of the DHR principle, adapted to the integrated circuits and MEMS technological constraints, is confirmed. In spite of the strong divergence of the light beam, the simulations show that the μ -PA sensor produces a pressure signal strong enough to match the next generation MEMS microphones resolution. This study also shows that the energy deposition localization does not have a major effect but that improving the coupling of light with gas in the chamber should be looked for. The detrimental influence of crosstalk, due to silicon transparency in the mid-IR, is moderate and is offset by the effortless suppression of the windows background.

The coupled model has already demonstrated its usefulness and will be further improved by taking into account the effect of the MEMS microphones in the viscothermal acoustic computation, as well as the microphone response and resolution. A crucial feedback will be provided by the characterizations and measurements performed on the prototype μ -PA cell currently in fabrication at CEA-LETI facilities.

Acknowledgments This research was supported by the French Agence Nationale de la Recherche (Project MIRIADE, ANR-11-ECOT-04) and by the Seventh Program Framework of the European Union (Project MIRIFISENS, FP7 317884). The authors gratefully acknowledge valuable comments from M. Brun, J. Czarny, S. Nicoletti, and A. Walther from CEA, LETI, MINATEC Campus.

References

1. J. Hodgkinson, R.P. Tatam, *Meas. Sci. Technol.* **24**, 012004 (2013)
2. A. Elia, P.M. Lugarà, C. Di Franco, V. Spagnolo, *Sensors* **9**, 9616 (2009)
3. M.W. Sigrist, *Air Monitoring by Spectroscopic Techniques* (Wiley, New York, 1994)
4. A. Miklos, P. Hess, Z. Bozoki, *Rev. Sci. Instrum.* **72**, 1937 (2001)
5. Y. Yao, A.J. Hoffman, C.F. Gmachl, *Nat. Photonics* **6**, 432 (2012)
6. M. Carras, G. Maisons, B. Simozrag, M. Garcia, O. Parillaud, J. Massies, X. Marcadet, *Appl. Phys. Lett.* **96**, 161105 (2010)
7. A.A. Kosterev, Y.A. Bakhirkin, R.F. Curl, F.K. Tittel, *Opt. Lett.* **27**, 1902 (2002)
8. S. Firebaugh, K. Jensen, M. Schmidt, *J. Appl. Phys.* **92**, 1555 (2002)
9. E.L. Holthoff, D.A. Heaps, P.M. Pellegrino, *IEEE Sens. J.* **10**, 572 (2010)
10. A.V. Gorelik, A.L. Ulasevich, F.N. Nikonovich, M.P. Zakharich, V.A. Firago, N.S. Kazak, V.S. Starovoitov, *Appl. Phys. B* **100**, 283 (2010)
11. P. Karioja, K. Keraenen, K. Kautio, J. Ollila, M. Heikkinen, I. Kauppinen, T. Kuusela, B. Matveev, M.E. McNie, R.M. Jenkins, J. Palve, in *Optical Sensing and Detection*, ed. by F. Berghmans, A. Mignani, C. Hoof (SPIE—The International Society for Optical Engineering, Bellingham, WA, 2010).
12. A. Glière, J. Rouxel, B. Parvitte, S. Nicoletti, V. Zéninari, in *17th International Conference on Photoacoustic and Photothermal Phenomena (ICPPP17)* (2013).
13. V. Zeninari, V.A. Kapitanov, D. Courtois, Y.N. Ponomarev, *Infrared Phys. Technol.* **40**, 1 (1999)

14. S. Barbieri, J. Pellaux, E. Studemann, D. Rosset, *Rev. Sci. Instrum.* **73**, 2458 (2002)
15. M. Mattiello, M. Niklès, S. Schilt, L. Thévenaz, A. Salhi, D. Barat, A. Vicet, Y. Rouillard, R. Werner, J. Koeth, *Spectrochim. Acta. A Mol. Biomol. Spectrosc.* **63**, 952 (2006)
16. M. Carras, G. Maisons, B. Simozrag, V. Trinite, M. Brun, G. Grand, P. Labeye, S. Nicoletti, in *Photonic West* (SPIE—The International Society for Optical Engineering, Bellingham, WA, 2013), pp. 8631131–7.
17. H. Takahashi, A. Suzuki, E. Iwase, K. Matsumoto, I. Shimoyama, *J. Micromech. Microeng.* **22**, 8 (2012)
18. B. Baumann, M. Wolff, B. Kost, H. Groninga, *Appl. Opt.* **46**, 1120 (2007)
19. L. Duggen, N. Lopes, M. Willatzen, H.-G. Rubahn, *Int. J. Thermophys.* **32**, 774 (2011)
20. B. Parvitte, C. Risser, R. Vallon, V. Zéninari, *Appl. Phys. B Lasers Opt.* **111**, 383 (2013)
21. M. Feit, J. Fleck, *Appl. Opt.* **17**, 3990 (1978)
22. A.V. Prokhorov, *Metrologia* **35**, 465 (1998)
23. J. Mayrwöger, P. Hauer, W. Reichl, R. Schwodiauer, C. Krutzler, B. Jakoby, *IEEE Sens. J.* **10**, 1691 (2010)
24. L. Novotny, B. Hecht, *Principles of Nano-Optics* (Cambridge University Press, Cambridge, 2006)
25. A. Miklos, P. Hess, *Anal. Chem.* **72**, 30A (2000)
26. E.L. Holthoff, P.M. Pellegrino, J.S. Crompton, K.C. Koppenhoefer, in *Chemical, Biological, Radiological, Nuclear, and Explosives (CBRNE) Sensing XII*, ed. by A. Fountain, P. Gardner (SPIE—The International Society for Optical Engineering, Bellingham, WA, 2011).
27. P.M. Morse, K.U. Ingard, *Theoretical Acoustics* (Princeton University Press, Princeton, 1987)
28. L.B. Kreuzer, in *Optoacoustic Spectroscopy and Detection* (Academic Press, London, 1977), pp. 1–25.
29. L. Duggen, R. Frese, M. Willatzen, *J. Phys. Conf. Ser.* **214**, 012036 (2010)
30. W.R. Kampinga, Y.H. Wijnant, A. de Boer, *Acta Acust. United Acust.* **97**, 618 (2011)
31. W.M. Beltman, *J. Sound Vib.* **227**, 555 (1999)
32. N. Joly, *Acta Acust. United Acust.* **96**, 102 (2010)
33. M. Malinen, M. Lyly, P. Raback, A. Karkkkainen, L. Karkkainen, in *Proceedings 4th European Congress on Computational Methods in Applied Sciences and Engineering* (2004).
34. V. Zeninari, B. Parvitte, D. Courtois, V.A. Kapitanov, Y.N. Ponomarev, *Infrared Phys. Technol.* **44**, 253 (2003)
35. P. Robert, V. Nguyen, S. Hentz, L. Duraffourg, G. Jourdan, J. Arcamone, S. Harrison, in *2009 IEEE Sensors* (2009), pp. 963–966.